Chapter 3 Enhancement in electrical and magnetic properties with Ti-doping in $Bi_{0.5}La_{0.5}Fe_{0.5}Mn_{0.5}O_3$

3.1   Introduction

In recent years, multifunctional materials have attracted valuable interest due to the coexistence of more than one ferroic or anti-ferroic properties (like ferromagnetic, ferroelectric, ferroelastic, etc.) in the single-phase sample [9]. Among these multiferroics, the materials possessing ferroelectric (anti-ferroelectric) and ferromagnetic (anti-ferromagnetic) properties are called the magnetoelectric compound. In a ME compound, application of an external electric field can induce magnetization and application of a magnetic field can induce intrinsic polarization. The coupling between these properties for a ME compound makes them important not only for industrial application but also from the physics point of view for their improved physical properties [14, 22]. The co-existence of electric and magnetic ordering in multiferroic materials provides the potential application in data-storage systems, multiple-state memories, high energy density capacitors and in the field of Spintronics [84].

Among the discovered multiferroic materials only BFO exhibits ferroelectricity (T_C~1103 K) and G-type canted anti-ferromagnetism (T_N ~ 643 K) simultaneously above room temperature [31, 34]. It is distorted perovskite material with *R3c* space group [85]. Moreover, BFO is the type-I multiferroic compound (type-I multiferroics exhibit ferroelectric transition at a temperature T_C higher than the ferromagnetic transition temperature T_N, *i.e.,* $T_C > T_N$) as ferroelectric and magnetic order parameters have different sources. The single pair electrons in 6*s* orbital in Bi are responsible for ferroelectricity, while partially filled d-orbital of Fe lead to magnetic ordering in BFO. However, the high leakage current and low resistivity of the BFO which is due to the presence of Fe^{+3} and oxygen vacancies [33, 86], structural instability and the lack of formation of single phase, have restricted BFO to its limited applications. In order to

solve these problems of BFO extensive research had been done by partial substitution of the Bi- and Fe-sites of BFO. Extensive research in the past few years revealed that the suitable dopant substitutions (e.g., lanthanides such as La, Dy, Sm, etc.) improve the multiferroic properties of BFO [35, 87]. For example; La substitution for Bi can increase the dielectric constant in BFO and decrease the antiferromagnetic Neel temperature (T_N) [88]. Chauhan et al. observed that the structural phase transition in 15% Mn doping at Fe site of BFO, due to the distortion in the rhombohedral structure resulted in significant enhancement in magnetization [61]. However, co- doping is a much more efficient way to improve the multiferroic properties of BFO [89]. Huang et al. have reported the structural transition, and enhanced ferroelectricity in Ca and Mn co- substituted BFO thin films up to 10% substitution [89] and Li et al. and Xu et al. improved the ferromagnetism of BFO by doping Mn and Mg [90].

As discussed earlier, suitable substitution at Bi- and Fe-sites of BFO significantly improves the multiferroic properties of BFO. It may affect T_C and T_N, or it remains insensitive to both, or it may affect only one of the T_C. In this chapter, we have replaced 5% of Mn in $Bi_{0.5}La_{0.5}Fe_{0.5}Mn_{0.5}O_3$ compound with Ti by using conventional solid state reaction method and study the various aspects of the materials. This study may explore much new innovatory with respect to the replacement of 5% Ti at the Mn site of $Bi_{0.5}La_{0.5}Fe_{0.5}Mn_{0.5}O_3$.

3.2   Experimental Technique

Polycrystalline $Bi_{0.5}La_{0.5}Fe_{0.5}Mn_{0.5-x}Ti_xO_3$ samples were prepared by conventional solid state reaction method. Highly pure oxides, viz. Bi_2O_3, Fe_2O_3, La_2O_3, TiO_2, and MnO_2 were mixed in the stoichiometric ratio for about 1 h and calcined in a programmable furnace at 850 °C for 24 h.

Obtained samples were heat treated at 950 °C for 12 h and then quenched at room temperature. Structural characterizations were performed on compound having stoichiometric formula$Bi_{0.5}La_{0.5}Fe_{0.5}Mn_{0.5-x}Ti_xO_3$ (with x=0 and where x= 0.05) by X-ray diffractometer (Model: Miniflex-II, Rigaku, Japan) with CuKα radiation (λ = 1.5406 Å) for phase identification. Rietveld refinement of X-ray powder diffraction data was done with Full Prof program. Raman spectra were taken with a Renishaw micro-Raman spectroscope in the range of 200 cm^{-1} to 800 cm^{-1} using 514.5nm Ar^+ laser as excitation source. Dielectric measurements have been done with Agilent E4980A Precision LCR meter. The magnetization measurements were performed using a commercial superconducting quantum interference device [Magnetic Properties Measurement System XL-7, Quantum Design, Inc.] magnetometer. Systematic X-ray photoemission spectroscopy (XPS) experiments carried out on $Bi_{0.5}La_{0.5}Fe_{0.5}Mn_{0.5-x}Ti_xO_3$ (x=0, 0.05) compounds using Omicron Multi-probe surface science system; equipped with monochromatic source (XM 1000) and a hemispherical electron energy analyzer (EA 125). Throughout the photoemission experiments carried out at an average vacuum of ~4.0×10^{-11} Torr with power 300 Watt. The total energy resolution, estimated from the width of the Fermi edge, was about 0.25 eV for monochromatic Al Kα line with photon energy 1486.70 eV. The pass energy for survey scan core level spectra was kept at 50 and 30 eV respectively. Ar-ion sputtering performed at 2 KeV by maintaining extractor pressure 25mPa.

3.3   RESULTS AND DISCUSSION

3.3.1   X-ray diffraction analysis

Single phase BFO belongs to rhombohedral distorted perovskite structure with space group *R3c*. Cycloid spin structure in BFO prevents the observation of any net magnetization, which hinders the applicability of this material; otherwise, it is very promising material. 20% doping of rare earth La^{3+} ions in Bi site suppresses this cycloid spin structure and releases the locked spin, which eventually results in the enhanced value of magnetization. The destruction of the modulated spin structure has been related with the structural transition from rhombohedral *R3c* to orthorhombic *Pnma* due to the doping of La [58, 91]. We have also observed the orthorhombic *Pnma* structure in $Bi_{0.8}La_{0.2}FeO_3$ in our previous work. Further doping of 10% of Mn in Fe site does not change the structure and system remain orthorhombic *Pnma* [92]. In this work, we have synthesized La and Mn co-doped and La, Mn and Ti co-doped BFO samples. Rietveld refinement of the X-ray diffraction (XRD) patterns for La and Mn co-doped BFO and La, Mn and Ti co-doped BFO samples are shown in Figure 3.1. All peak positions of Ti-doped $Bi_{0.5}La_{0.5}Fe_{0.5}Mn_{0.5}O_3$ which correspond to the standard Bragg positions of orthorhombic structure (space group *Pnma*) are shown by the vertical bars and the residue by the curved line respectively. Figure 3.1 shows that the Ti-doping causes to create no extra peak (like Fe_2O_3, Fe_3O_4, Fe, $Bi_2Fe_4O_9$, etc.) or disappearance of any peak of the orthorhombic structure of pure $Bi_{0.5}La_{0.5}Fe_{0.5}Mn_{0.5}O_3$ at least to the detection limit of XRD. It confirms that the structure of the doped $Bi_{0.5}La_{0.5}Fe_{0.5}Mn_{0.5}O_3$ remains orthorhombic belonging to the space group *Pnma*.

Thus, the Rietveld analysis shows that the samples are of single phase and no trace of other impurities has been found.

Lattice parameters of $Bi_{0.5}La_{0.5}Fe_{0.5}Mn_{0.5}O_3$ and $Bi_{0.5}La_{0.5}Fe_{0.5}Mn_{0.45}Ti_{0.05}O_3$ obtained from Rietveld refinement are $a = 5.5543$ Å, $b = 7.8349$ Å, $c = 5.5427$ Å and $a = 5.5554$ Å, $b = 7.8256$ Å, $c = 5.5434$Å respectively, while $\alpha=\beta=\gamma=90°$ in both cases. Lattice volumes of $Bi_{0.5}La_{0.5}Fe_{0.5}Mn_{0.5}O_3$ and $Bi_{0.5}La_{0.5}Fe_{0.5}Mn_{0.45}Ti_{0.05}O_3$ calculated from given values are 241.2052 Å^3 and 240.9933 Å^3 respectively.
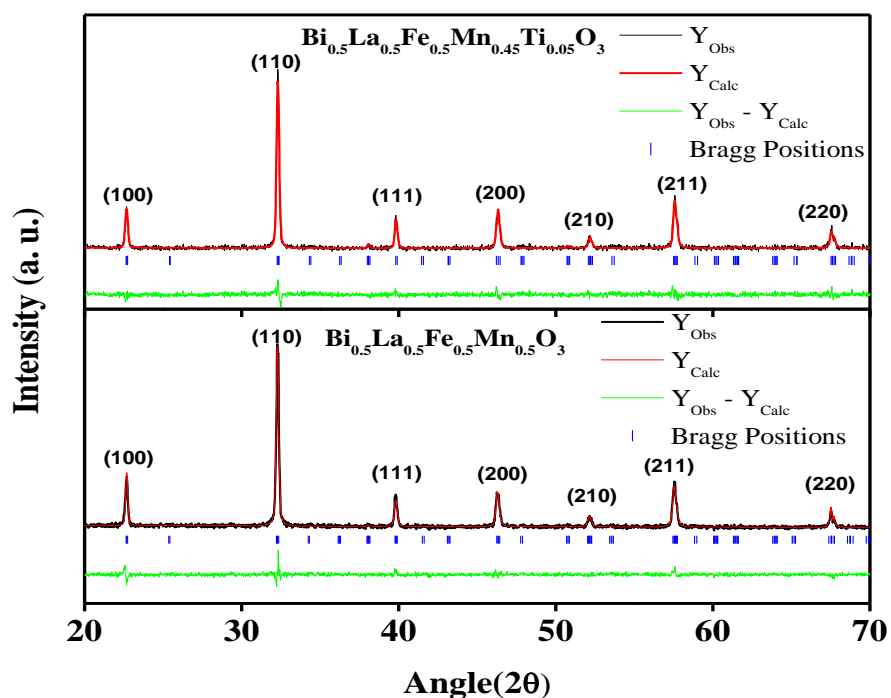

Figure 3.1 Rietveld refinement profiles of X-ray diffraction patterns of $Bi_{0.5}La_{0.5}Fe_{0.5}Mn_{0.5}O_3$ and $Bi_{0.5}La_{0.5}Fe_{0.5}Mn_{0.45}Ti_{0.05}O_3$ samples. The dots represent the observed data while solid line through dots s the calculated profile, vertical tics below curves represent allowed Bragg-reflections for the wurtzite phase. The difference is given below the vertical tics.

3.3.2   Raman Spectroscopy

Raman spectroscopy is considered to be the most powerful nondestructive technique to study the crystalline quality, structural transition (arising due to doping of the rare earth elements) and defects in the host lattice. Theoretical analysis revealed eighteen (18) optical phonon modes: Γ_{opt} = $4A_1 + 5A_2 + 9E$ for BFO at room temperature in which A_1 and E modes (13) both are Raman active modes whereas the A_2 modes (5) are IR active for rhombohedral distorted *R3c* BFO] [92, 93]. Yuan *et al.* observed that out of those 13 possible Raman modes, their rhombohedral distorted BFO sample showed only 9 Raman modes, which according to irreducible representation are assigned as; A_1-1, A_1-2, A_1-3, E-2, E-3, E-4, E-5, E-6, and E-7 at 126.1, 165.5, 213.0 , 259.5 , 339.6, 366.6, 476.9, 530.9, and 599.6 cm^{-1} respectively [49].Yuan *et al.* reported 10 Raman modes for $Bi_{0.5}La_{0.5}Fe_{0.5}Mn_{0.5}O_3$ viz. E1, A_1-1, A_1-2, A_1-3, E-3, E-4, A_1-4, E-5, E-6 and E-7 have been observed at near 221, 284, 315, 410, 477, 535, and $650 cm^{-1}$ respectively. We clearly observed only three intense Raman modes for $Bi_{0.5}La_{0.5}Fe_{0.5}Mn_{0.5}O_3$ and $Bi_{0.5}La_{0.5}Fe_{0.5}Mn_{0.45}Ti_{0.05}O_3$ in the range of 200 cm^{-1} to $1000 cm^{-1}$ as shown in Figure 3.2. It is due to the fact that Raman spectra of sample depend on the size of the unit cell and the number of the atoms in the unit cell. Usually, small unit cell and a limited number of the unit cell shows all the Raman modes as expected from symmetry argument and vice-versa. The Ti-doped $Bi_{0.5}La_{0.5}Fe_{0.5}Mn_{0.5}O_3$ slightly shifts to high frequency because the frequency of the mode is proportional to $(k/M)^{1/2}$, where k is the force constant and M is the reduced mass. The average mass of the B-site significantly decreases with the substitution of Ti because the atomic mass of Ti is about 87% of that of Fe. $Bi_{0.5}La_{0.5}Fe_{0.5}Mn_{0.45}Ti_{0.05}O_3$ has almost the same Raman pattern as $Bi_{0.8}La_{0.2}Fe_{0.9}Mn_{0.1}O_3$. The presence of the weak modes A_1-3 (at~220 cm^{-1}) and E-2 (at ~255

cm^{-1}) which are governed by Bi–O covalent bonds, [93] experience very slow shifts in frequency as observed in our study gives rise tono effect on structural change. Hence, there is no further structural phase change due to the Ti–substitution.
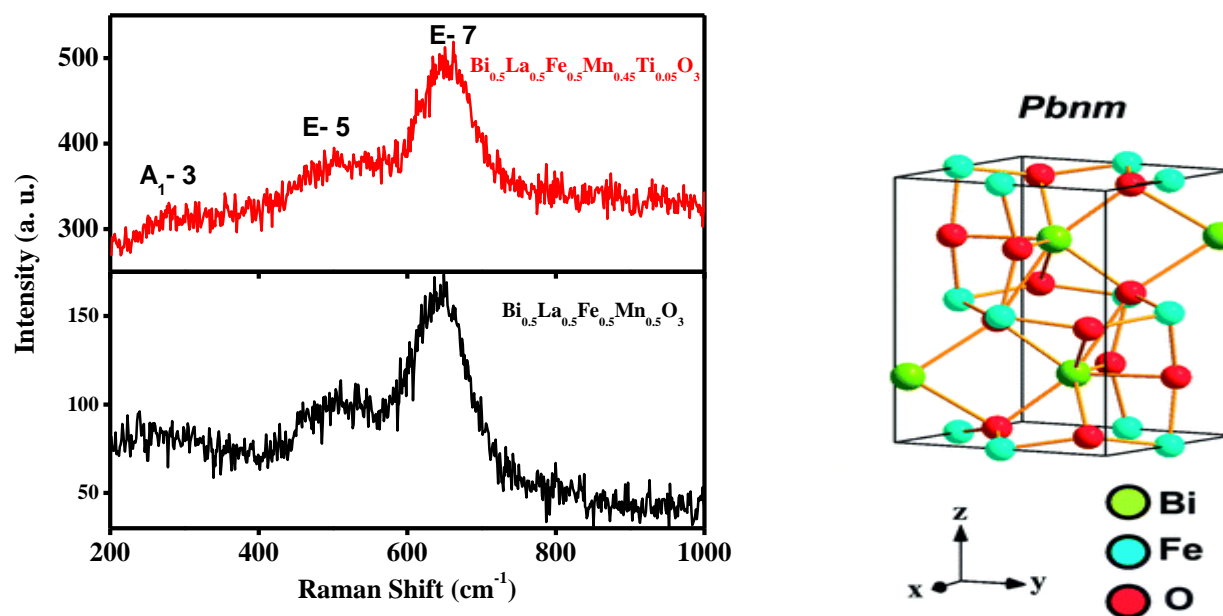

Figure 3.2 Room-temperature micro-Raman spectra of (a) $Bi_{0.5}La_{0.5}Fe_{0.5}Mn_{0.5}O_3$ and (b) $Bi_{0.5}La_{0.5}Fe_{0.5}Mn_{0.45}Ti_{0.05}O_3$ samples.

3.3.3 Magnetic property

The magnetic hysteresis (M–H) loops of $Bi_{0.5}La_{0.5}Fe_{0.5}Mn_{0.5}O_3$ and $Bi_{0.5}La_{0.5}Fe_{0.5}Mn_{0.45}Ti_{0.05}O_3$ at different temperatures (2K, 80K, and 300K) have been shown in Figure 3.3(a and b). The M-H hysteresis loop observed for both systems is deviated from linearity indicating the appearance of ferromagnetism in $Bi_{0.5}La_{0.5}Fe_{0.5}Mn_{0.5}O_3$ and $Bi_{0.5}La_{0.5}Fe_{0.5}Mn_{0.45}Ti_{0.05}O_3$ samples. This non-linear behavior of the hysteresis loop has been reported earlier for $Bi_{0.8}La_{0.2}FeO_3$ and $Bi_{0.8}La_{0.2}Fe_{0.9}Mn_{0.1}O_3$ [92]. The evolution of weak ferromagnetism in substituted samples is accounted due to the canting of antiferromagnetically ordered spins which result in the

enhancementof remnant magnetization and coercivity for substituted BFO samples. The non-linear behavior of the M-H loop had been measured earlier for $Bi_{0.5}La_{0.5}Fe_{0.5}Mn_{0.5}O_3$ up to magnetic field ($\pm$ 5T).

The magnetization, remnant magnetization and coercivity obtained for $Bi_{0.5}La_{0.5}Fe_{0.5}Mn_{0.5}O_3$ are 2.9 emu/g, 0.7 emu/g, and 2259.9 Oe respectively at 2K. Substitution of 5% Ti at Fe site replaces Mn-ions shows a decrease of magnetization. The magnetization and remnant magnetization decrease to 1.9 emu/g and 0.4 emu/g respectively while coercivity increases to 3638.2Oe at 2K. This decrement of magnetization might be due to the substitution of nonmagnetic Ti^{4+} ion at the Fe site because Ti^{4+} cation has electronic configuration [Ar] $3d^0$, which clearly shows the absence of unpaired electrons. The amplitude of χ'_{ac} is strongly reduced upon doping of Ti at Mn-site.
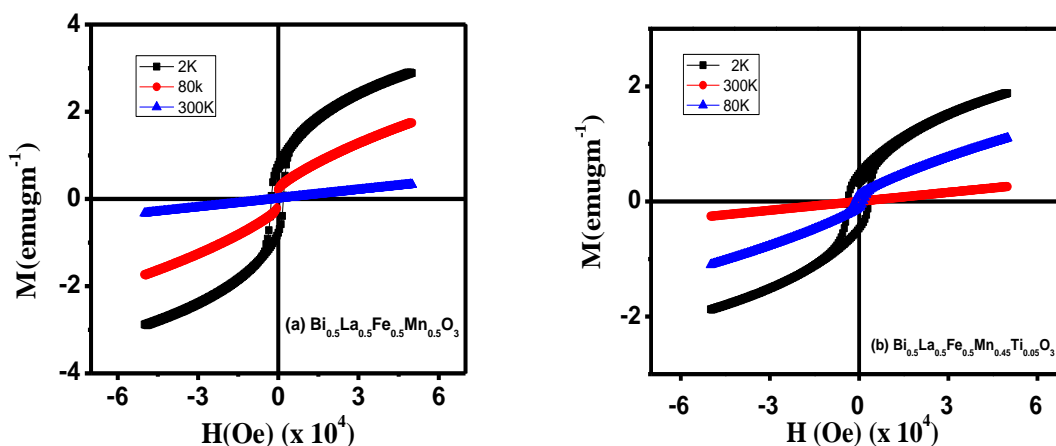

Figure 3.3. Magnetization vs. applied magnetic field variation of (a) $Bi_{0.5}La_{0.5}Fe_{0.5}Mn_{0.5}O_3$ and (b) $Bi_{0.5}La_{0.5}Fe_{0.5}Mn_{0.45}Ti_{0.05}O_3$.
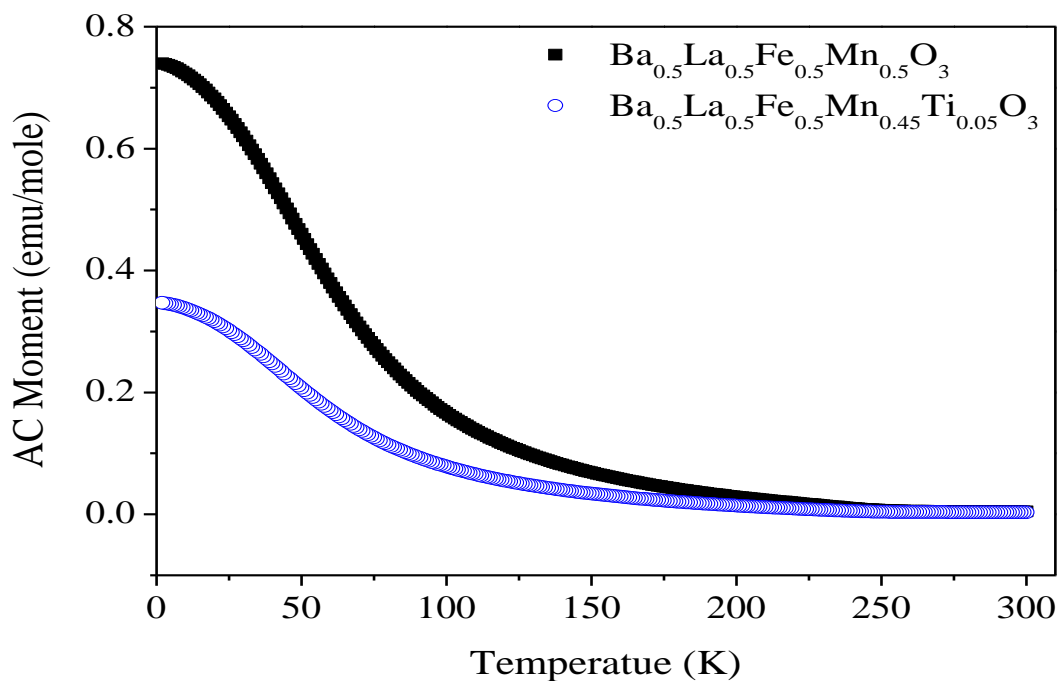
Figure 3.4 Temperature dependence of the in-phase component of ac susceptibility measured under a field of 500 Oe under the field-cooled condition for $Bi_{0.5}La_{0.5}Fe_{0.5}Mn_{0.5}O_3$ and $Bi_{0.5}La_{0.5}Fe_{0.5}Mn_{0.45}Ti_{0.05}O_3$.

3.3.4 XPS study

To obtain the core electronic structure of $Bi_{0.5}La_{0.5}Fe_{0.5}Mn_{0.5}O_3$ and $Bi_{0.5}La_{0.5}Fe_{0.5}Mn_{0.45}Ti_{0.05}O_3$ we have performed X-ray photoemission spectroscopy (XPS) studies on them. Figure 3.5 and 3.6 show their respective electronic structures. All the peak positions have been indexed according to the National Institute of Standards and Technology (NIST) XPS database [94]. The survey scans (Figure 3.5 (a) and Figure 3.6 (a)) confirm the presence of the constituent atoms i.e., Bi, La, Fe, Mn, Ti & O and also confirm the absence of any foreign element present in the compound. The peak C1s is present due to the surface adsorbed C atoms coming from the atmosphere and occurs quite commonly in the XPS spectra of many compounds. Being surface adsorbed, the C atoms have no influence on the bulk physical properties reported in this study. The different core levels

for both these compounds show multiple features arising due to spin-orbit splitting, mixed valency and/or various final state effects. Figure. 3.5 (b) and 3.6 (b) show splitting of the Bi4f level into a doublet Bi4$f_{7/2}$ and Bi4$f_{5/2}$ which is due to the spin-orbit splitting. The La3d spectra show similar spin-orbit splitting into La3$d_{5/2}$ and La3$d_{3/2}$ peaks however every individual peak is further split into a doublet. This is explained as a result of the final state effect arising due to the different photo-hole screening channels available via the bonding and antibonding states of the La valence electrons [94]. The two peaks are due to the occupancy of La 4f state into 4f^0 and 4f^1 configuration in the final state of the core hole [94] The Fe3s and Mn3s core levels in both the compounds are shown to be separated by a weak and broadened feature (*) which could be a loss feature associated with core levels or it also could be the magnetic exchange split Mn3s feature due to intra-atomic exchange coupling of Mn3s electron with Mn3d electron. In the latter case, the Mn3s doublet gives an energy separation of $\Delta E \approx 5.47$ eV which corresponds mainly to a trivalent state of [Mn] [94] which is also confirmed from the relative peak areas under the Mn^{4+} and Mn^{3+} peaks of the Mn2p core level. The Ti2p level in case of the Ti-doped compound shows a weak intensity, as expected, with a spin-orbit splitting and largely interferes with the Bi4$d_{3/2}$ peak at the Ti2$p_{1/2}$ peak position. The two peaks around 457.65 eV and 465.3 eV correspond to the spin-orbit splitting doublet Ti2$p_{3/2}$ and Ti2$p_{1/2}$respectively, which confirms the Ti-ion substitution at Mn-site. The Fe2p and Mn2p core levels show a doublet splitting of the individual spin-orbit split peaks (i.e., 2$p_{3/2}$ and 2$p_{1/2}$) arising due to Fe^{2+} (lower B.E.) & Fe^{3+} (higher B.E.) and Mn^{3+} (lower B.E.) and Mn^{4+} (higher B.E.) respectively. Furthermore, shakeup satellites corresponding Fe^{3+} state are visible in the spectra for both the compounds suggesting the

dominant presence of Fe^{3+} state in the compound] [95]. Please note that Fe^{3+} is more magnetic (~5.92 μ_B) than Fe^{2+} (~4.90 μ_B) potentially contributing to the observed ferromagnetism.
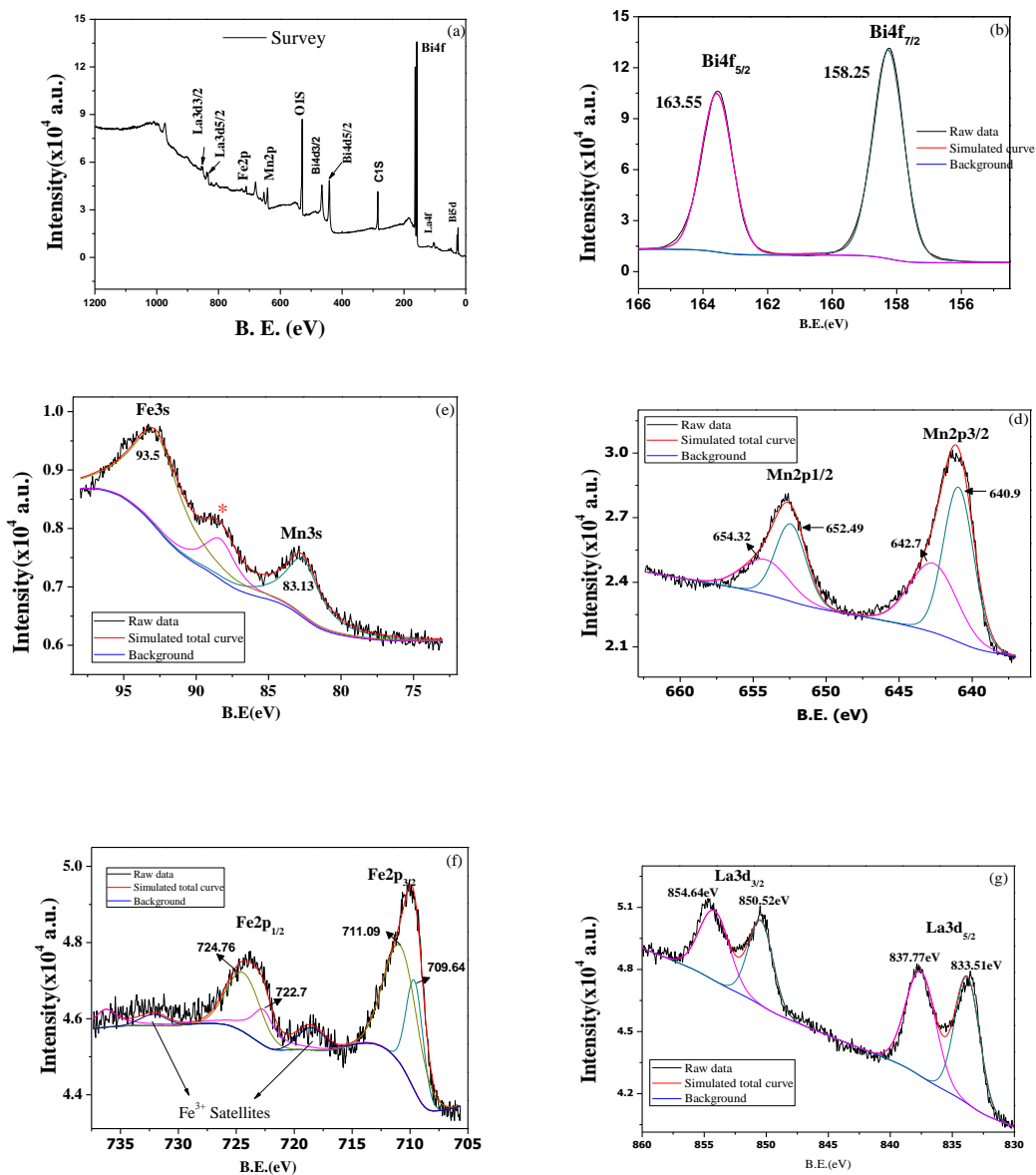

Figure 3.5. (a) Survey scan (b) Bi4f, (c) Fe2p, (c) Fe3s and Mn3s, (d) Mn2p, (f) Fe2p and (g) La3d core level X-ray photoemission spectra for Bi0.5La0.5Fe0.5Mn0.5O3 at 300 K.
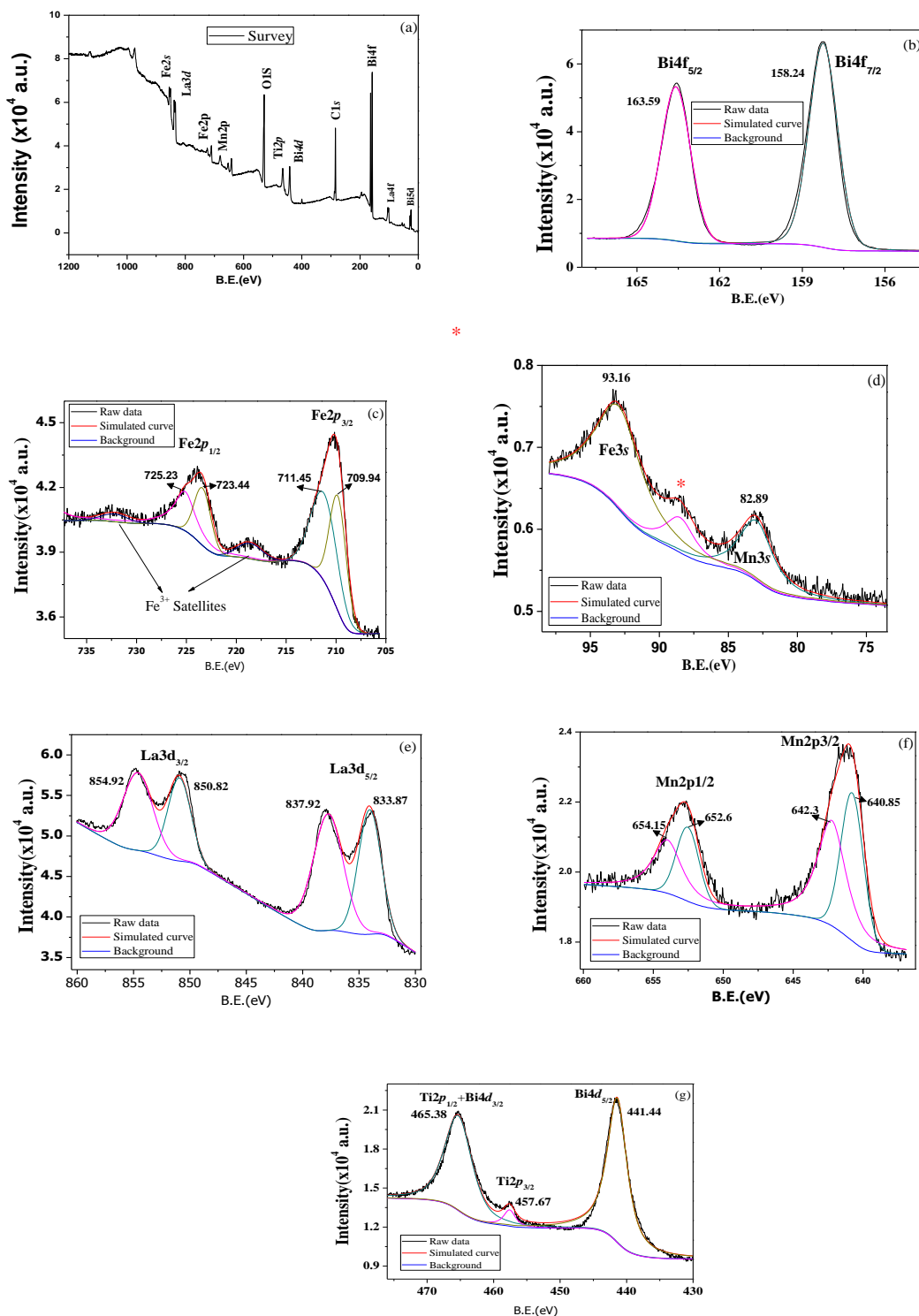
Figure 3.6 (a) Survey scan, (b) Bi4f, (c) Fe2p, (d) Fe3s and Mn3s, (e) La3d, (f) Mn2p, and (g) Ti2p and Bi4d core level X-ray photoemission spectra for Bi0.5La0.5Fe0.5Mn0.45Ti0.05O3 at 300 K.

3.3.5　Dielectric Properties

The temperature dependence of the real part of the dielectric constant (ε') and dielectric loss (tanδ) at different frequencies (1 kHz – 2 MHz) for $Bi_{0.5}La_{0.5}Fe_{0.5}Mn_{0.5}O_3$ and $Bi_{0.5}La_{0.5}Fe_{0.5}Mn_{0.45}Ti_{0.05}O_3$ are shown in Figure. 3.6. The relative dielectric permittivity was calculated using the relations:

$$\varepsilon' = Cd/\varepsilon_0 A$$

Where C is the capacitance of the measured sample in Farad, d is the thickness of the sample in meters, and A is the cross section area of the sample and ε_0 is the permittivity of free space (8.854×10^{-12} Fm^{-1}).

$$\varepsilon'' = \varepsilon' \tan \delta$$

Where, ε'' is the dielectric loss and tanδ is the loss tangent.

As we see from the Figure above a certain temperature, (above 200K in the case of $Bi_{0.5}La_{0.5}Fe_{0.5}Mn_{0.5}O_3$ and 170 K in $Bi_{0.5}La_{0.5}Fe_{0.5}Mn_{0.45}Ti_{0.05}O_3$) ε' increase sharply and shows a high dielectric constant with weak-temperature dependence. As the frequency increases this temperature also increase. Around room temperature ε' ~8.5×10^3 for $Bi_{0.5}La_{0.5}Fe_{0.5}Mn_{0.5}O_3$ while in the case of $Bi_{0.5}La_{0.5}Fe_{0.5}Mn_{0.45}Ti_{0.05}O_3$ the value of ε' ~1.5×10^4 increases significantly. This is due to the fact that at low temperature electric dipoles freeze though relaxation process, so there is decay in polarization with respect to applied electric field but at higher temperature polarization increases due to the thermally excited relaxation process. Further, a large increase in the dielectric loss which is accompanied for greatly enhanced in dielectric constant verify

Maxwell–Wanger relaxation mechanism [95, 96]. We have done the low temperature dielectric measurements, so antiferromagnetic Neel transitions do not appear in this temperature range. In both system, dielectric constant decrease with the increase in frequency. But Ti substituted $Bi_{0.5}La_{0.5}Fe_{0.5}Mn_{0.5}O_3$has low leakage current, large dielectric constant ε' and dielectric loss (tanδ). The reason behind this Ti-doping increases defects near the grain boundary so the probability of inter-well hopping increase which result in large dielectric relaxation at low frequency [96]. At higher frequency, the intra-well hopping probability of charge carries dominates.
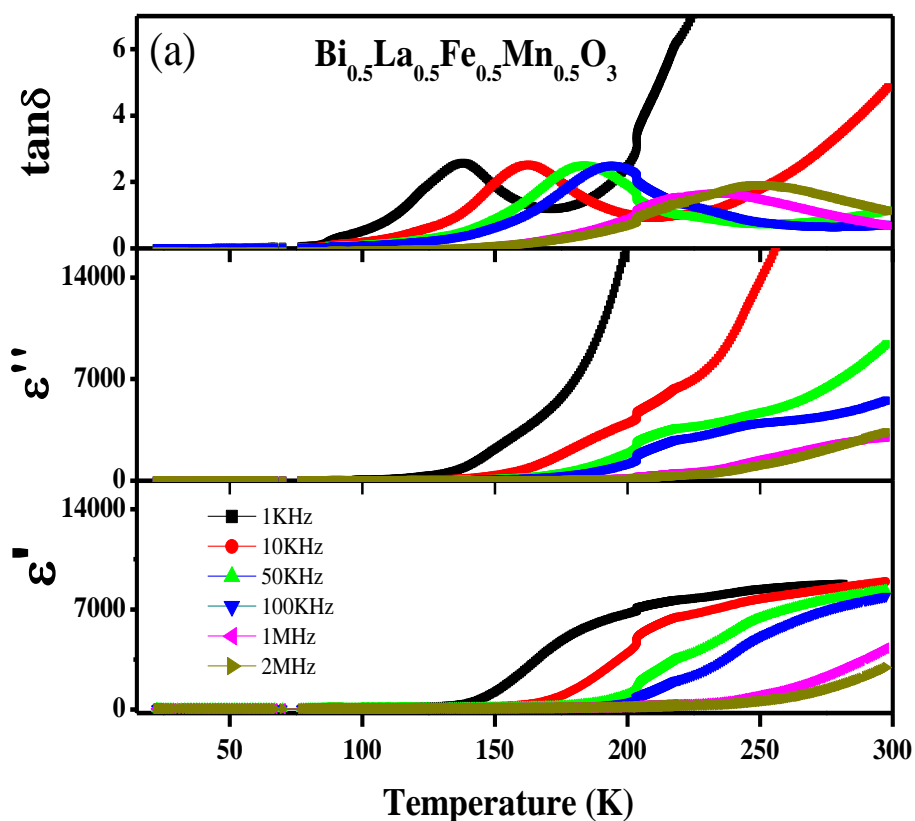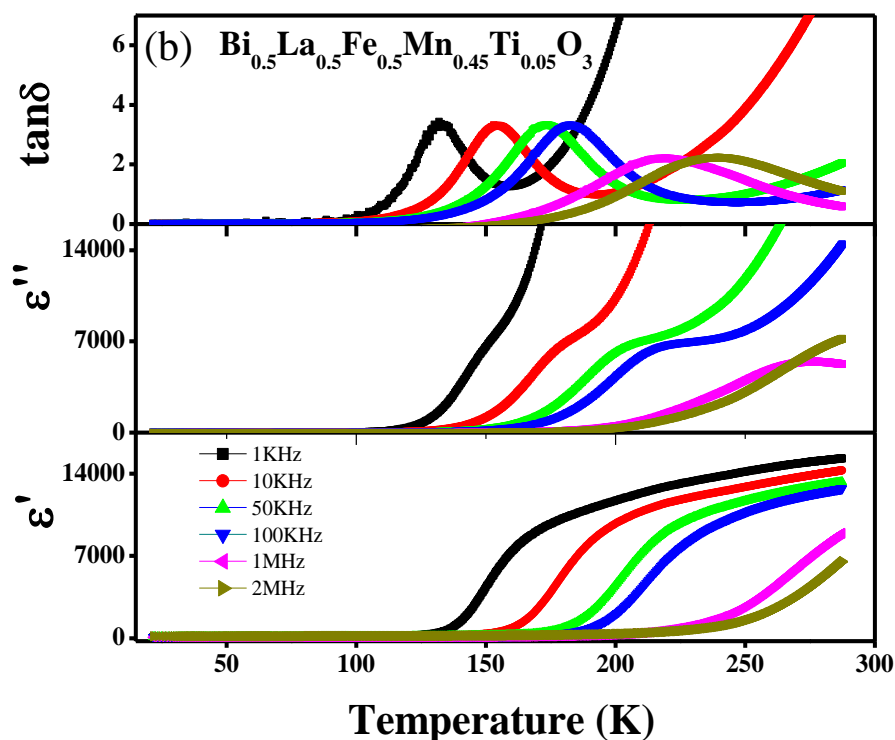
Figure 3.7. Variation of ε′ and tan(δ) with respect to temperature at 1kHz , 10khz , 50kHz , 100kHz,1MHz and 2MHz for (a)Bi$_{0.5}$La$_{0.5}$Fe$_{0.5}$Mn$_{0.5}$O$_3$ and (b) Bi$_{0.5}$La$_{0.5}$Fe$_{0.5}$Mn$_{0.45}$Ti$_{0.05}$O$_3$.

3.4 Conclusions

In this chapter we have systemically studied the structural, magnetic and dielectric study of Bi$_{0.5}$La$_{0.5}$Fe$_{0.5}$Mn$_{0.5}$O$_3$ and Ti-substituted Bi$_{0.5}$La$_{0.5}$Fe$_{0.5}$Mn$_{0.5}$O$_3$ by using different experimental techniques. The XRD with Rietveld refinement and micro-Raman analysis shows that Ti-doped Bi$_{0.5}$La$_{0.5}$Fe$_{0.5}$Mn$_{0.5}$O$_3$ have orthorhombic *Pnma* structure which indicates that Ti-ions have substituted the Mn ions. X-ray Photoemission study confirms the presence of all elements in the compound. Oxidation state of Mn exists in mixed valence state (3+/4+), while it confirms the substitution of Ti in the compound with 4+ valence state. The evolution of weak ferromagnetism is observed in Ti-substituted samples is accounted due to the canting of antiferromagnetically

ordered spins which results in enhancement of remnant magnetization and coercivity for substituted BFO samples. Dielectric measurement shows that ε' increases sharply and shows high dielectric constant with weak-temperature dependence. At room temperature, the value of ε' ~8.5×10^3 for $Bi_{0.5}La_{0.5}Fe_{0.5}Mn_{0.5}O_3$ while in the case of $Bi_{0.5}La_{0.5}Fe_{0.5}Mn_{0.45}Ti_{0.05}O_3$ the value of ε' ~1.5×10^4 showing a significant increase with Ti doping.